Robotica (2024), **42**, pp. 2511–2527
doi:10.1017/S0263574724000900

CAMBRIDGE UNIVERSITY PRESS

RESEARCH ARTICLE

Closed-loop control of a tendon-driven active needle for tip tracking at desired bending angle for high-dose-rate prostate brachytherapy

Samuel Lafreniere, Blayton Padasdao and Bardia Konh

Department of Mechanical Engineering, University of Hawaii at Manoa, Honolulu, HI, USA
Corresponding author: Bardia Konh; Email: konh@hawaii.edu

Received: 6 December 2023; **Revised:** 2 May 2024; **Accepted:** 4 May 2024; **First published online:** 27 August 2024

Keywords: control of robotic systems; mechatronic systems; surgical robots; sensor or actuator design; design

Abstract

Prostate cancer is the second most common malignancy in American men. High-dose-rate brachytherapy is a popular treatment technique in which a large, localized radiation dose is used to kill cancer. Utilization of curvilinear catheter implantation inside the prostate gland to provide access channels to host the radiation source has shown superiority in terms of improved dosimetric constraints compared to straight needles. To this aim, we have introduced an active needle to curve inside the prostate conformal to the patient's specific anatomical relationship for improved dose distribution to the prostate and reduced toxicity to the organs at risk. This work presents closed-loop control of our tendon-driven active needle in water medium and air using the position feedback of the tip obtained in real time from an ultrasound (US) or an electromagnetic (EM) tracking sensor, respectively. The active needle consists of a compliant flexure section to realize bending in two directions via actuation of two internal tendons. Tracking errors using US and EM trackers are estimated and compared. Results show that the bending angle of the active needle could be controlled using position feedback of the US or the EM tracking system with a bending angle error of less than 1.00 degree when delay is disregarded. It is concluded that the actuation system and controller, presented in this work, are able to realize a desired bending angle at the active needle tip with reasonable accuracy paving the path for tip tracking and manipulation control evaluations in a prostate brachytherapy.

1. Introduction

1.1. Challenges associated with needle insertion tasks

Several minimally invasive diagnostic and therapeutic procedures rely upon needle insertion techniques. The procedures' success rate depends on accurate navigation of the steerable needles and precise tip placement at target locations. Limited needle actuation and flexibility inside tissue, movement of the target during needle insertion [1], and inadequate visualization with the most practiced ultrasound (US) and magnetic resonance imaging (MRI) inside of the patient's body [2] are cited as common challenges in manual or robotic needle placement.

An example of a minimally invasive procedure that benefits from accurate needle placement is prostate brachytherapy. Prostate cancer is the second most common cancer among men in the U.S. [3] with an estimated 288,300 new cases and 34,700 deaths in 2023 [4]. High-dose-rate (HDR) brachytherapy is an internal and temporary radiotherapy method to remove cancerous tumors. Conventional HDR brachytherapy involves placement of radiation sources close to the tumor using rigid, straight needles. Although the conventional method has been promising [5–9] in terms of tumor control, toxicities, overall costs, and effectiveness (e.g., 5-yr and 10-yr distant metastasis-free survival rates) [10–14], studies have reported side effects such as edema in tissue, incontinence, and impotence. The side effects are a result of excessive radiation and needle penetration into sensitive organs such as the urethra, bladder, rectum, penile bulb, cavernous veins, and neuro-vascular bundles. Also, use of HDR brachytherapy is

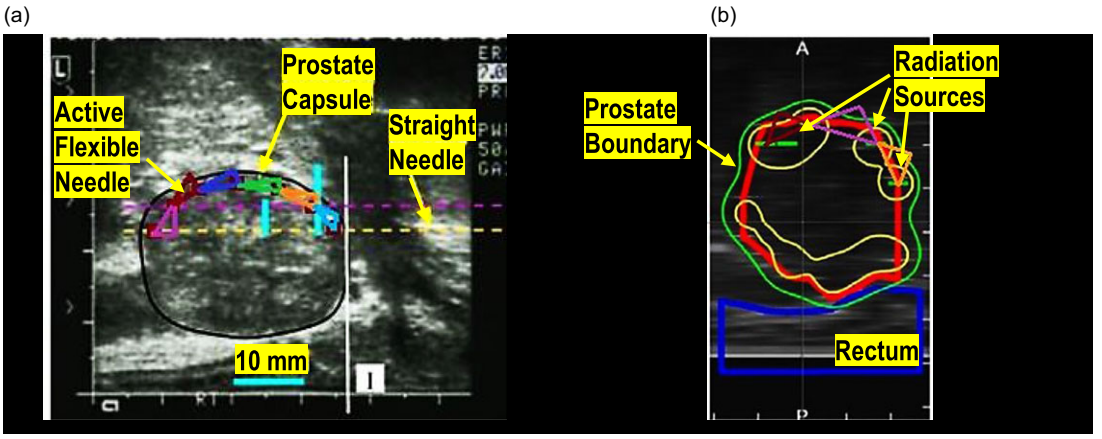

Figure 1. *Straight vs. curved trajectories for needle insertion inside (a) Undeformed, and (b) Deformed prostate.*

limited in patients whose pubic arch obstructs the transperineal path to the prostate, thereby interfering with needle placement [15]. A study showed that the procedure was practical only for 24 out of the 40 patients studied due to pelvic bone arch interference [16]. Even a narrow pubic arch may prevent proper implantation in a small prostate gland [17]. Known strategies to overcome this problem such as oblique catheter insertion and pelvic rotation [18, 19] are not optimal. Active tendon-driven needles [20, 21] have shown promises to alleviate this concern via their precise navigation in desired trajectories.

On another note, imprecise catheter implantation often causes insufficient dosage to the cancer and/or inadvertent radiation of the rectum, urethra, and bladder. The former causes failure of treatment, while the latter results in adverse side effects like rectal ulceration, incontinence, and dysuria (painful urination). Increased doses to normal structures are well correlated with increased toxicity after brachytherapy, and despite the adoption of modern techniques, toxicity remains significant [22]. We have previously introduced [23, 24] a new Curvilinear Catheter Implantation (CuLCI) method for the purpose of enabling dose escalation to the dominant intraprostatic lesion, while reducing toxicity to organs at risk (OARs). Our previous studies with 20 patients have shown significant dose improvement using the CuLCI method with fewer needle insertions.

Figure 1a & 1b show a US image of an anonymized patient's prostate gland, where the boundaries of the prostate are marked by a urologist. In conventional prostate brachytherapy, needles are inserted in straight trajectories (examples are shown in Fig. 1a with dashed lines) using conventional straight and rigid needles; however, conformal to the patient's specific anatomy (shown in the figure with small triangles) are curved trajectories that are feasible to achieve using active flexible needles. Noting that most of the cancers are located in the peripheral zone of the prostate, placing radiation source(s) in nearby areas (marked in Fig. 1b via the curved access channels of the active needles) is of great interest. In addition, active flexible needles provide the opportunity to move away from OARs such as urethra, bladder, and rectum and thereby lower the risk of excess toxication. Fig. 1b shows the prostate of the same patient when deformed due to a needle insertion. The small triangles in both figures are used to estimate the range of bending angle that an active needle should realize in a needle insertion task.

1.2. Background and related work

In the past decade, there has been notable advancement in the development and control of flexible needles. For example, a flexible and steerable needle was designed and developed in ref. [25] to navigate a planar arc through soft tissue, targeting multiple points with minimal damage. In another work [26], a closed-loop control method was presented for bevel-tip needles, improving precision and reducing

trauma through multi-objective optimization. Purposed for lung biopsy, a flexible robot was developed to enhance endoscopic surgery capabilities with its cable-driven mechanism to reach target nodules through narrow and tortuous pathways [27]. In another recent study, contact forces were estimated for continuum robots using local curvatures demonstrated high accuracy with fiber Bragg gratings (FBG) sensors [28]. Konh et al. [29] explored the use of shape memory alloy (SMA) actuators to manipulate an active needle in 3D space, while non-model-based control methods for an SMA-actuated needle were explored in ref. [30], highlighting the effectiveness of the robust adaptive proportional-integral-derivative (PID) sliding mode controller.

Dexterity and visualization of robotic instruments are key factors in the procedure's success. Recent research has been focused on improving *flexibility* of the instruments as well as *sensing and visualization* of the instruments inside the body. Examples of robotic tools with improved flexibility include continuum robots [31], concentric tubes [32, 33], 3D-printed active flexible needles [34, 35], notched needles [36, 37], and steerable guidewires [38]. To the best of our knowledge, none of the above-mentioned active needles are specifically designed and developed for prostate brachytherapy.

Besides needle actuation, intraoperative tracking of the needle and tissue is of great importance. Robotic closed-loop control of the needles navigating inside tissue relies on the feedback of the needle tip position and/or the needle shape. Since the needles should ultimately perform percutaneous procedures in nontransparent human tissue, vision-based (camera) tracking is unrealistic. On the other hand, use of position or shape sensors is not desired due to the small (meso-scale) size of the needle. Thus, US or MRI imaging feedback is ideal candidates for needle tip and shape tracking; however, intraoperative image acquisition and processing to have reliable feedback in real time is challenging. Concerning efforts related to imaging modalities, an MRI-compatible system has been developed [39] with a hybrid tracking method that eliminated the need for performing manipulator motions inside the scanner while still retaining accuracy. Our group has developed a robotic platform [40, 41] to operate an active needle inside MRI bore for MR image-guided interventions. In another work, a method was proposed [42] to estimate a passive needle tip's trajectory using 2D transverse US images.

Recent research efforts have introduced needle-tissue interaction models to predict the needle behavior inside tissue. For example, a mechanics-based dynamic model was introduced [43] to estimate deflection of a bevel-tip flexible needle while inserted into soft tissues. In a later study, an overview of this dynamic model was presented with comments about controllability of flexible needle insertions [44]. In another work [45], a needle insertion model with mechanics of tissue rupture, and effect of insertion velocity on needle force, tissue deformation, and needle work, was presented. Another study in 2012 [46] introduced a mechanics-based model for needle deflection with multiple bends during insertion into soft tissue based on a Rayleigh-Ritz formulation. In later study, in 2015 [47], the beam theory was extended to develop a new mechanics-based dynamic model for needle insertion in soft tissue. More recent works [48, 49] presented an estimator to predict needle tip deflection and needle shape during needle insertion into soft tissue. Finite element methods have also been developed to model needle-tissue interactions using a discretized model of the needle and tissue [50, 51]. A nonholonomic model for steering flexible needles with bevel tips was developed in ref. [52] for needle control with actuations at the base of the needle. Another study in 2015 [53] presented an extension to the kinematic bicycle model for bevel-tipped needle motion in soft tissue, accounting for non-constant curvature paths for the needle tip. Our group has recently introduced [54, 55] a model for active needle insertions in soft tissue. The models are intended to be used in model-based control of the needle while navigating inside tissue toward a moving target. However, models are associated with errors, and could not be trusted without additional sensory feedback and a proper controller. This work presents real time and reliable estimation of the needle tip to realize a closed-loop control of the needle movement inside tissue.

Several sensing and visualization techniques have also been developed to provide feedback to the operating surgeon of the robotic systems. Recent progress in sensing and visualization of the robotic tools include US tip tracking [56– 58], shape prediction [59–61], FBG based force estimation and shape sensing [62, 63] and SMA self-shape and self-force sensing [64, 65]. Our group has previously published works on needle actuation. In one work, we studied the performance and interactive response of multiple

distributed SMA actuators to manipulate a 3D-printed active flexible needle [66]. In another work, we developed an electrical resistance feedback control of multiple SMA actuators to control the movement of a 3D steerable active needle [67] in a tissue phantom.

This work presents two tendon-driven active needles to achieve a robotic bidirectional bending inside tissue. The active needle consists of a flexure section (FS), carefully designed, for improved flexibility inside the prostate gland. The needle's bidirectional bending is realized via independent actuation of two internal tendons. A closed-loop control is designed and implemented to use real-time US tracking in water medium and electromagnetic (EM) tracking in air as position feedback of the needle's tip for closed-loop control. Ultimately, the performance of the active needle in a water medium is evaluated to assess if the US tracking system can provide reliable position feedback to the controller for precise needle manipulation. The contribution of this work lies in its unique needle design, tailored specifically for HDR brachytherapy, coupled with the utilization of efficient control methods relying on EM or ultrasonic position feedback.

This manuscript is organized as follows: Section 1 provides an introduction to the needle insertion tasks and their challenges (Section 1.1), along with the background and related works in this area (Section 1.2). Section 2 lays out our robotic and control methods to improve the needle insertion tasks. Section 2.1 introduces our tendon-driven active needle, while Sections 2.2 and 2.3 cover the actuation system to manipulate the active needle with US and EM tracking systems, respectively. Section 2.4 explains our closed-loop control method with a disturbance observer for precise manipulation of the active needle. Section 3 summarizes the results, with discussions on the tendon displacement control in Section 3.1, and the active needle response using the US and EM tracking systems in Sections 3.2 and 3.3, respectively. Discussions and conclusions are outlined in Sections 4 and 5, respectively.

2. Materials and methods

2.1. Robotic tendon-driven active needle

The design of the tendon-driven active needle is shown in Fig. 2a. The active needle was developed by carving a series of six small notches on each side of a superelastic nitinol tube (Johnson Matthey, London, UK). Schematic dimensions of each notch are shown in Fig. 2b with the corresponding values listed in Table 1.

The notches produce a FS, shown in Fig. 2a, that allows for improved flexibility of the active needle. Two holes (0.25 mm in diameter) were made near the distal end of the FS for two tendons (0.10 mm diameter SMA wires) to get attached to. The tendons were looped in and out of the holes and completely fixed to drive needle bending when pulled.

Two active needles were developed in this work, with two different FSs, using the following manufacturing methods (i) ultraviolet (UV) laser cutter machine (Confluent Medical, Scottsdale, AZ) on the nitinol tube with 1.49 mm inner diameter (ID) and 2.00 mm outer diameter (OD) shown in Fig. 2c, henceforth called FS I, and (ii) typical machining methods in lab on the nitinol tube with an ID of 1.60 mm and OD of 2.00 mm shown in Fig. 2d, henceforth called FS II.

The notches on the FS I were developed with a width of 0.46 mm and a depth of 1.68 mm, achieving enhanced flexibility through increased precision, however at higher manufacturing cost. The notches on the FS II were created in the laboratory using a Dremel, with dimensions of around 0.42 mm in width and 1.33 mm in depth, all achieved at a relatively low production cost. In contrast, FS I demonstrates superior fatigue properties when compared to FS II.

The FS of the active needle was sealed to prevent tissue penetration into the needle tube and avoid tissue rupture. Shown in Fig. 2c, the FS was covered (tight fit) with a polyethylene terephthalate (PET) heat shrink tube (13 μm thickness). The PET material is biocompatible and sterilizable with ethylene oxide. We have tested the heat shrink tube on the active needle when bent and inserted into phantom tissues to ensure that it does not rip off during an insertion task [68]. The active needle including the covered FS is sterilizable.

Table I. *The dimensions of the notches for the two active needles developed in this work. Units are in mm.*

	r_i(ID)	r_o(OD)	d	t
FS I	0.75 (1.49)	1.00 (2.00)	1.68	0.46
FS II	0.80 (1.60)	1.00 (2.00)	1.33	0.42

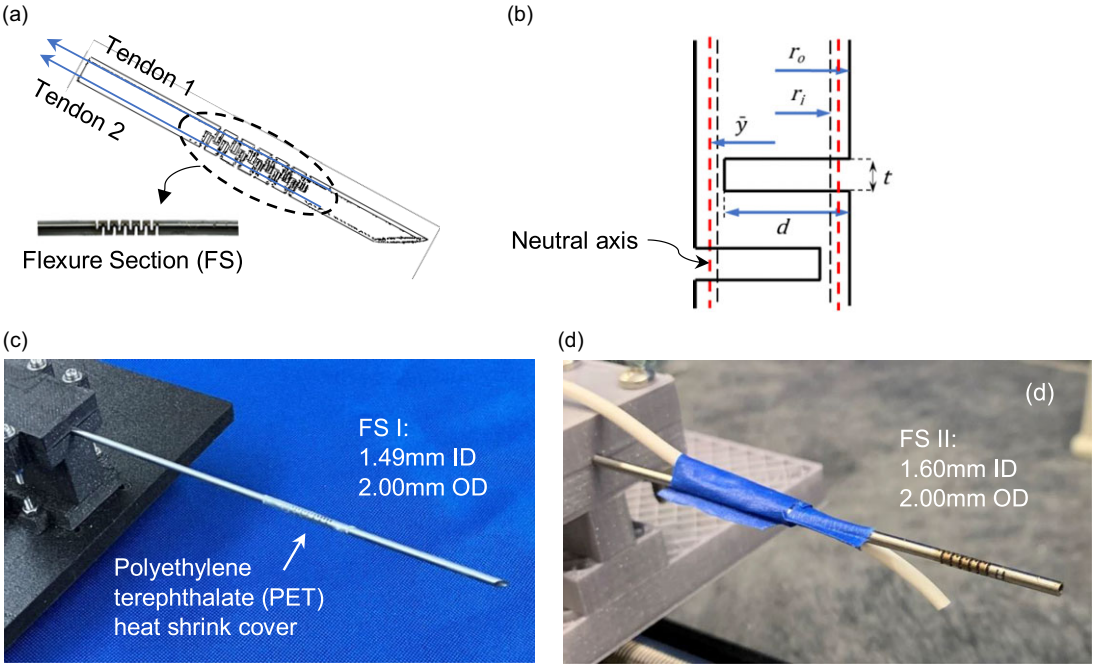

Figure 2. *Schematic design of (a) Tendon-driven active needle with (b) The notch dimensions that are fabricated on a nitinol tube using UV laser cutter and typical machining in our laboratory to develop two flexure sections (FSs) shown in (c) FS I and (d) FS II, respectively.*

The utmost expected angular deflection of the active needle to realize a curved trajectory inside prostate gland was estimated using Fig. 1b, where a small radius of curvature is desired inside a deformed prostate. The bending angles were marked in the figure with small triangles on the curved trajectory, and the largest overall angular deflection of 50 degrees was measured. Methods to estimate the bending angles of the two active needles, developed in this work, are explained below.

The following equations are used to estimate the bending angle of the FS. For the notches schematically shown in Fig. 2b, the neutral bending axis is estimated using the following equation [69]:

$$\bar{y} = \frac{4(r_o{}^3 \sin^3(\phi_o) - r_i{}^3 \sin^3(\phi_i))}{3\,(r_o{}^2\,(2\phi_o - \sin 2\phi_o) - r_i{}^2\,(2\phi_i - \sin 2\phi_i))} \tag{1}$$

where $\bar{y}$ is the distance moved from the center of the tube, r_o and r_i are the outer and inner radii of the tube, respectively, and ϕ_o and ϕ_i are found by the following equations:

$$\phi_o = \arccos\left(\frac{d - r_o}{r_o}\right) \tag{2}$$

$$\phi_i = \arccos\left(\frac{d - r_o}{r_i}\right) \tag{3}$$

where d is the notch depth. The bending angle for each notch can be estimated as:

$$\theta_i = \frac{h}{r_o + \bar{y}} \tag{4}$$

where h is the height of the neutral axis for each, which in this work is equal to the height of the cut (t). Assuming that the total deflection is distributed equally among the six notches, the bending angle of the whole flexible section could be found by multiplying the bending angle of each notch by the number of notches.

Dimensions of each notch for the two FSs are listed in Table 1. Using the equations above, the angular deflections of each notch were 14.48 and 14.13 degrees for the FS I and FS II, respectively. The overall angular deflections of the FSs (six notches) were 86.88 and 84.78 degrees for the FS I and FS II, respectively, which both surpass the expected angular deflection of 50 degrees for the active needle.

2.2. Actuation and ultrasound tracking system

The actuation system designed in this work consists of a motor, gear box, and lead screw. The tendon pulling force (F) to realize a specific bending on the FS when bending inside tissue should be estimated experimentally. The following equation is used to calculate the amount of torque (T) required to pull the tendon and consequently bend the active needle, similar to lowering a load on a lead screw:

$$T = \frac{F d_m}{2}\left(\frac{l + \pi f d_m \sec\alpha}{\pi d_m - f l \sec\alpha}\right) \tag{5}$$

where $d_m, l, f,$ *and* α are the mean diameter of a single thread, tendon displacement, coefficient of friction, and thread angle, respectively. To provide an example of calculations for the active needle (shown in Fig. 1b), we estimated that a maximum of 22N of force (tendon pulling force) is sufficient to bend the needle inside the tissue. This was estimated through needle insertion experiments in tissue phantoms with different Young's modulus [70] resembling prostate tissue. With this tension, an 8 mm diameter lead screw, friction coefficient of 0.25 for threaded pairs of a steel and dry screw, and thread angle of zero for square threads, the maximum torque was estimated as 0.41 N.m. Upon torque estimation, a DC motor, gear, and a lead screw combination were selected and purchased to develop a pulling actuation mechanism. To realize bidirectional bending on the active needle, two similar tendon actuation mechanisms were developed and installed to have full control over needle bending.

The experimental setup to actuate the active needle at a desired bending angle and real-time US tracking in water medium is shown in Fig. 3a. The position of the tip is tracked using the US machine, processed through a series of image processing commands, and provided to the controller for appropriate control actions (explained later).

The actuation system to pull the internal tendons of the FS I to realize a desired bidirectional bending at the tip (shown in Fig. 3b) consists of two motors, each consisting of a 0.5W (Maxon Group, Sachseln, Switzerland) DC motor RE 8 Ø8 mm, Precious Metal Brushes with an 8 mm diameter lead screw drive (GP 8 S Ø8 mm, Metric spindle, M3 x 0.5), and an encoder (MR, Type S, 100CPT).

An L7 Linear Array US probe (CHISON Medical Technologies Co., Ltd., Jiangsu, China) was used to track the tip of the active needle in real time in water medium. The active needle was submerged in water with the US lying on the surface of the medium. For proper sealing, the inner walls of the 3D-printed box (made by Prusa i3 MK3 printer), shown in Fig. 3c, were coated with a silicone sealant (Gorilla Glue Co., Cincinnati, OH). To prevent water from entering the needle tube, wood putty (Minwax, Cleveland, OH) was used at the distal end surrounding the entry point of the needle.

Figure 3d shows the 2D plane of the US for tip tracking. The cross section of the needle appears as a circular shape in the US images. The US images are obtained in real time with a frame grabber, Epiphan Av.io HD. (Epiphan Systems, Ottawa, Canada) from the ECO 5 (CHISON Medical Technologies Co., Ltd., Jiangsu, China) through the US probe.

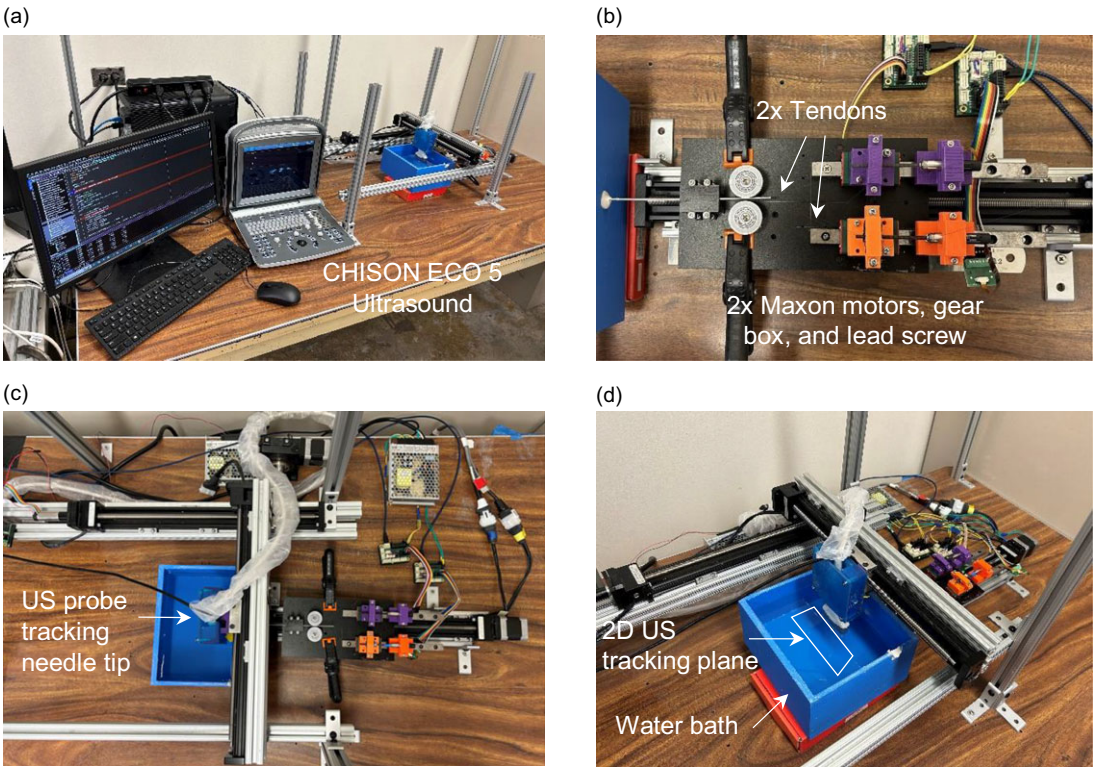

Figure 3. *Experimental setup to evaluate performance of the tendon-driven active needle in water medium consisting of (a) US tracking, (b) Tendon actuation system to bend the flexure section in two directions, (c) Active needle and US probe submerged in water bath, and (d) 2D US plane for tracking bidirectional movement of the active needle tip.*

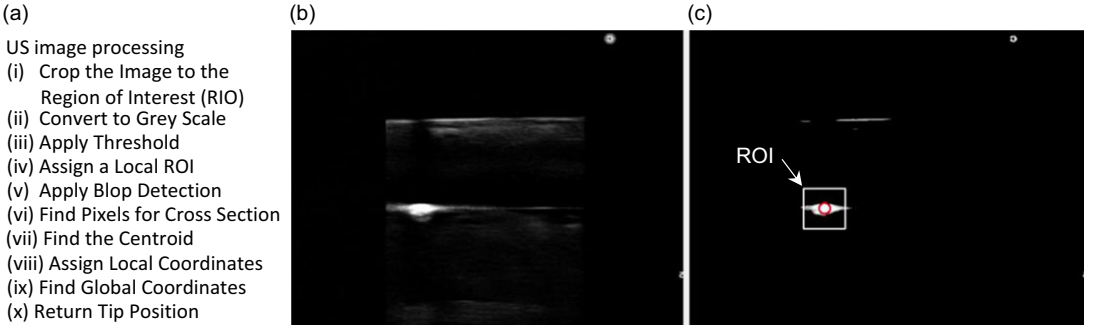

Figure 4. *(a) Image processing method showing (b) Unprocessed US images with sources of noise, and (c) Processed US images in real time. The tip is marked with a red circle.*

Due to the artifacts observed in the US images while tracking the needle movement in the water medium, a series of image processing techniques (Fig. 4a) were performed to obtain the 3D coordinates of the active needle tip in real time. Fig. 4b shows an unprocessed US image, while Fig. 4c shows the processed image where region of interest is designated by the white box with the needle tip being marked with a red circle. The script assigned a coordinate system for the y-z plane over the US image being generated, using the pixel count as a basis for converting to millimeter scaling.

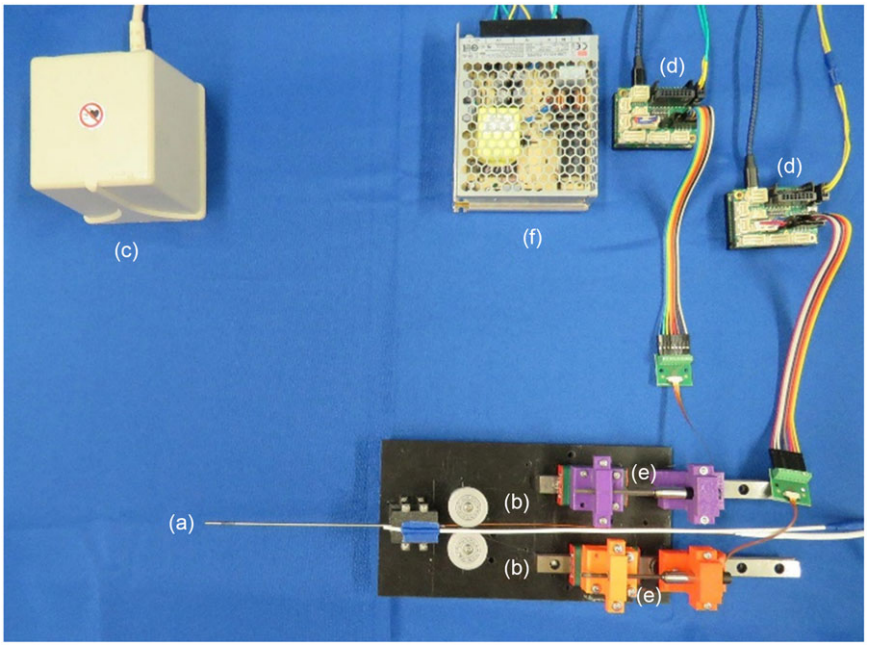

Figure 5. *Actuation and electromagnetic (EM) tracking system consists of (a) Active needle, (b) EM sensors, (c) EM transmitter, (d) EPOS4 positioning control boards, (e) Two Maxon motors, and (f) Power supply.*

2.3. Actuation and electromagnetic tracking system

Another method of tracking the needle tip position was developed in this work using two 3D Guidance Model 55 EM tracking sensors (Northern Digital Inc., Waterloo, Canada), shown in Fig. 5. The EM tracking system includes two sensors. The first and second sensors were installed inside the needle tube at the tip and the proximal end of the needle, respectively. The EM tracker reports displacement and rotation data, so the bending angle at the FS of the active needle is measured directly by measuring the rotation of the distal sensor compared to the stationary proximal sensor. A similar actuation system, using Maxon motors as explained above, was used to manipulate the active needle. Manipulation and control were performed in the air.

2.4. Closed-loop control

This section presents our controller to manipulate the tip of the active needle to follow a desired trajectory and reach a target point in water medium and air. Fig. 6 shows a schematic block diagram of our closed-loop control algorithm for US-based or EM-based tracking methods to realize a desired bending angle at the active needle's FS. The controller communicates with the actuation system to realize appropriate tendon displacements via actuation of the Maxon motors and consequently realizes an angular deflection at the FS of the active needle. The controller was programed to force the FS to follow an input desired bending angle function. The needle tip position obtained by the US tracking system, or the tip and distal positions of FS obtained by the EM tracking system, was recorded in real time and used to estimate the angular bending of the FS. The PID controller (explained below) compares the input desired function with the bending angle estimated obtained in real time from the US or the EM tracking system to adopt appropriate control actions.

To properly control the actuators to pull the internal tendons and consequently realize a desired bending angle at active needle tip, kinematic analysis of the FS is needed. The kinematic analysis provides

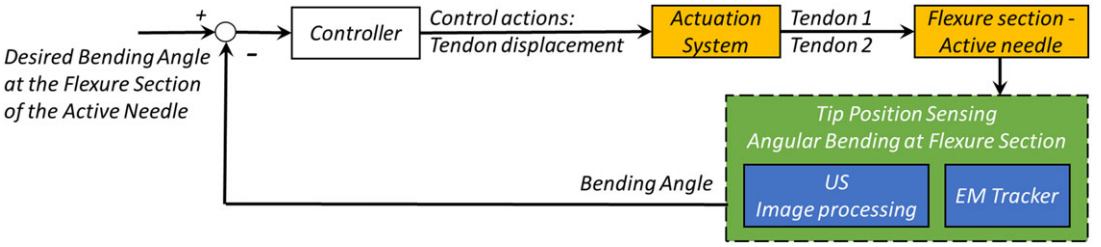

Figure 6. *Scheme of closed-loop control method to realize a desired bending angle at the flexure section of the active needle.*

a relationship between the tendon displacement and the bending angle. For the active needle, presented in this work, the kinematic analysis is as follows:

$$\Delta L = f\,(\theta, N, d) + \epsilon(\theta, d, t, N) \tag{6}$$

where ΔL is the tendon displacement, θ is the bending angle, N is the number of notches, d is the notch depth, and t is the gap between two consecutive notches. The first and second terms refer to the kinematic and the tendon elongation, respectively. The kinematic term is:

$$f\,(\theta, N, d) = N.r_t.\,\sin\,(\delta\theta) \tag{7}$$

where $\delta\theta$ is the bending angle of each notch, which is part of the total bending angle ($\theta = N.\delta\theta$), and r_t can be found by:

$$r_t = d - \frac{(OD - ID)}{2} - \frac{t_d}{2} \tag{8}$$

where OD is the outer diameter of the tube, ID is the inner diameter of the tube, and t_d is the diameter of the tendon. The tendon elongation term is approximated by:

$$\epsilon\,(\theta, d, t, N) = E_{tendon}.F_{tendon}(\theta, d, t, N) \tag{9}$$

where F_{tendon} is the tendon tension measured experimentally, and E_{tendon} is the tendon compliance approximated by the relationship between the tendon length (L_{tendon}), and the Young's modulus of the nitinol tendon (E_{tendon}) as:

$$E_{tendon} = \frac{L_{tendon}}{A.E_{tendon}} \tag{10}$$

For the active needles presented in this work, the parameters listed in Table 1 are fed into the equations. The relationship between the force and the bending angle, $F_{tendon}(\theta, d, t, N)$, is obtained experimentally as:

$$F_{tendon}\,(\theta, d, t, N) = 0.2743\theta \tag{11}$$

To realize a desired bending angle at the tip of the active needle, a closed-loop PID controller (shown in Fig. 7a) was designed and implemented.

In the system diagram, $\Delta\theta$ is the bending angle output of the active needle that is provided as a feedback in the closed-loop system, $\Delta\theta_{ref}$ is the reference (desired) bending angle with respect to the measured angle ($\Delta\theta$), e is the error of the system ($e = \Delta\theta_{ref} - \Delta\theta$), and ΔL is the tendon displacement. The transfer functions, shown in the system diagram, are K_i, $G_1(s)$, $G_2(s)$, and $G_3(s)$, that describe relationships between control input (u) vs. current (i), current (i) vs. actuator torque (τ), actuator torque (τ) vs. actuator stroke (ΔL), and actuator stroke (ΔL) vs. $\Delta\theta$, respectively. Since the electrical response of the actuator based on the current input is faster compared to other mechanical responses in the diagram, $G_1(s)$ is assumed as a constant value. $G_2(s)$ is designed as a second-order system. The linear stroke of the actuator (ΔL) is measured experimentally to build dynamics with respect to the actuator torque. The control error, e, is used as the input of the PID controller, producing the PID control input (u). $G_3(s)$

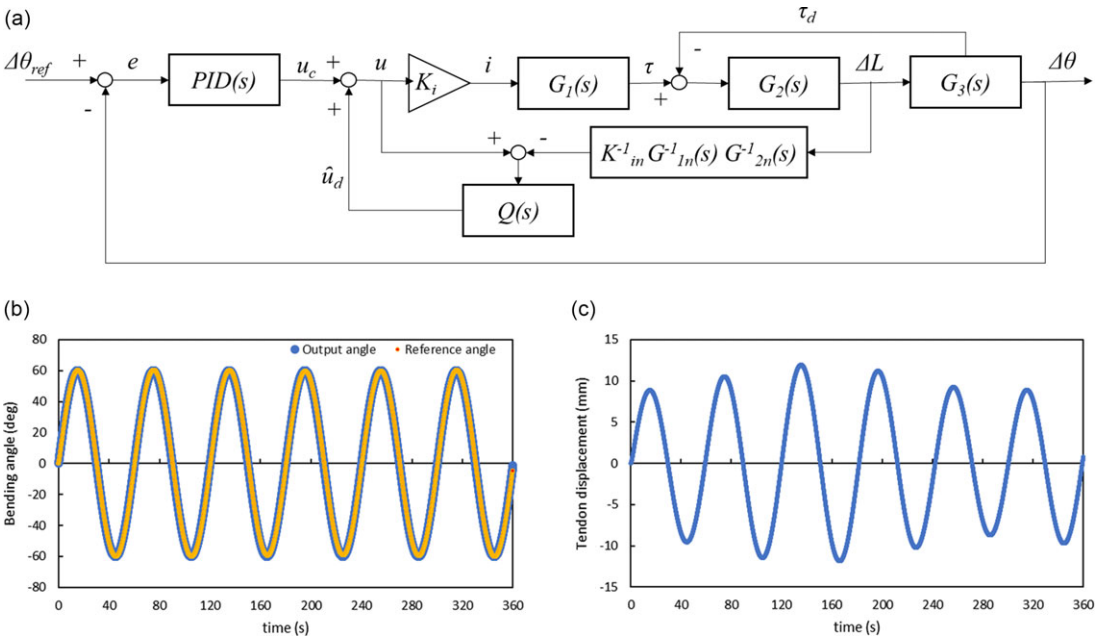

Figure 7. *(a) Closed-loop PID controller to realize a desired bending angle on the compliant flexure section, (b) Comparison between the reference (desired) and output bending angles, and (c) Tendon displacement simulated for the system input.*

represents the kinematic model of the active needle (described above). The relationship (and the transfer function) between ΔL and u could be found as:

$$\Delta L = (K_i)\, G_1\,(s)\, G_2(s)\,(u) \tag{12}$$

The system is subject to a disturbance torque (τ_d) imposed by the stiffness of the FS of the active needle on the motor, and thereby cannot have a consistent response. To avoid undesired responses (e.g., overshoot or non-consistent steady-state error) and to develop a precise and robust position controller, a disturbance observer was added to the PID controller. The disturbance observer loop estimates τ_d in form of a control input ($\hat{u}_d$) as:

$$\hat{u}_d = \left(u - \Delta L.K_{in}^{-1}.G_{1n}^{-1}.G_{2n}^{-1}\right) Q \tag{13}$$

where K_{in}^{-1}, G_{1n}^{-1}, and G_{2n}^{-1} are nominal forms of the functions, K_i, G_1, and G_2, respectively, which are estimated with the system identification toolbox (MATLAB R2022b, The Mathworks Inc.) from the measured response of these functions with respect to a chirp signal input, and Q is a second-order low-pass filter as $Q(s) = w_c^2/(s^2 + 2w_c s + w_c^2)$, where w_c is cutoff frequency. Then, $\hat{u}_d$ is added to u_c resulting in the control input, u:

$$u = u_c + u_d \tag{14}$$

The control algorithm was implemented in Simulink (The Mathworks Inc.) to tune the PID coefficients. The controller's capability to match the output angle to the reference (desired) angle was evaluated when the reference bending angle changed between $-60°$ and $+60°$. The simulation tuned the PID coefficients as P:1.2, I:5, and D:0.02. Fig. 7b compares the output angle ($\Delta\theta$) and the reference bending angle ($\Delta\theta_{ref}$), showing that the output follows the reference angle. Fig. 7c shows the tendon displacement that is set by the controller to reach the reference angle. Additional experimental tuning was required when implementing the closed-loop control on the active needles. This was done by careful observation of the effects of each coefficient on the overall performance of the system. The

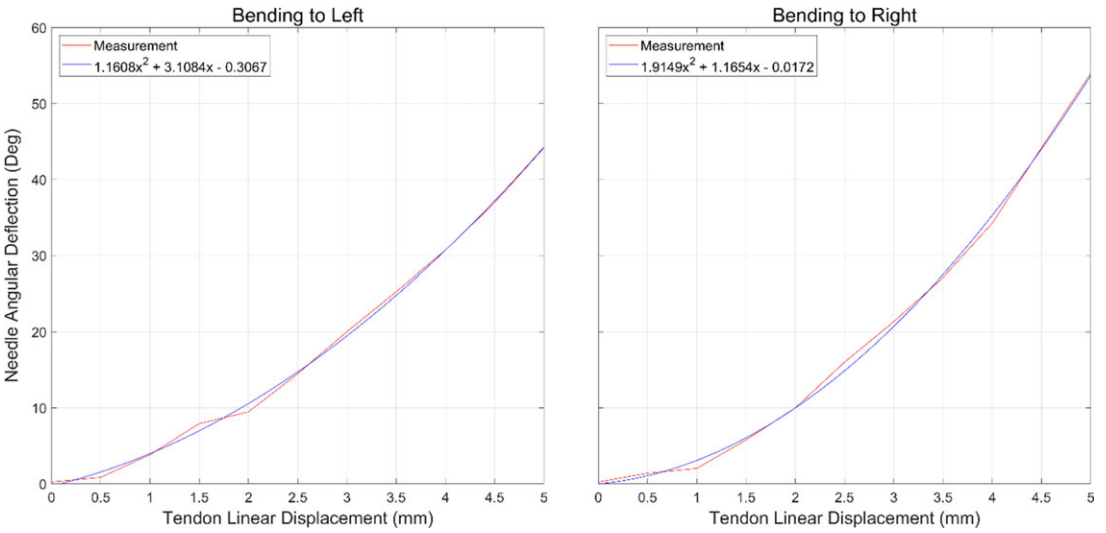

Figure 8. *Relationship between angular deflection of the flexure section and the tendons' linear displacement.*

proportional gain affects the speed of reaching the desired angle, the integral gain reduces the steady-state error, and the derivative gain reduces the overshoots. The experimentally tuned PID coefficients are P:0.45, I:0.0075, and D:0.5. The system oscillates between two close values (with $\pm 2^{\circ}$ error from the desired angle). Bending experiments were performed with the active needles and the actuation system to evaluate the controller.

3. Results

3.1. Relationship between the tendon displacement and angular deflection

To characterize the FS, the tendons were linearly and independently displaced at increments of 0.5 mm. Images were taken of the FS at each increment and the angular deflection was measured using ImageJ. Fig. 8 shows the relationship between the linear displacement of the tendon with the angular deflection (bending) of the FS toward opposite directions (left and right). A second-order polynomial function was fitted to the data to model the relationship between the tendon displacement and the angular deflection of the FS. This relationship was used by the controller to make decisions on the tendon displacement actions.

3.2. Closed-loop control with US tracking feedback

To evaluate the performance of the active needle as well as the capability of our US tracking system to provide reliable feedback, the controller was set to realize a maximum angular bending of 10 degrees in a water medium. The coordinates of the needle tip were displayed on a computer running the US tracking script and recorded for graphical analysis post-experimentation. The coordinates were used to calculate the bending angle of the FS in real time. Time was also recorded during the experiment. The measured bending angle (output), as well as the desired bending angle (input) determined by the displacement function, was also recorded, analyzed, and compared. Three different input bending angle functions of (i) step, (ii) sine, and (iii) triangle were utilized for the FS to follow. The actual (green) and desired (red) bending angle of the FS was compared (Fig. 9a) and the corresponding absolute difference (bending angle error) between the measured output and desired input was estimated and plotted (Fig. 9b).

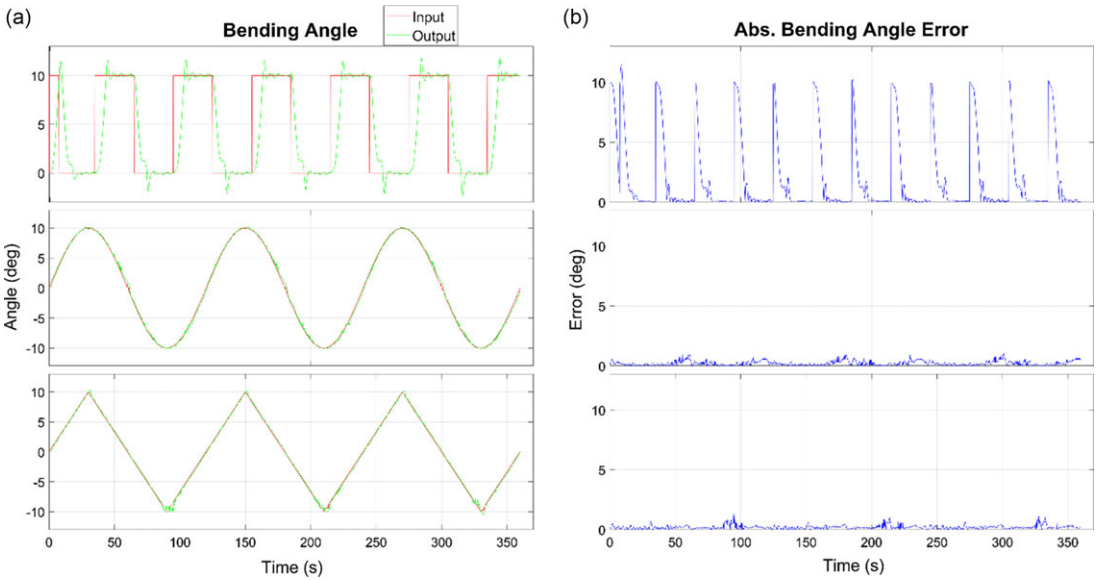

Figure 9. *Bending angle of the tendon-driven active needle: (a) Calculated from the data collected by the US tracking system for the different input functions, and (b) Corresponding absolute difference (bending angle error) with respect to time.*

3.3. Closed-loop control with EM tracking feedback

To test the capability of the EM tracking system, the same displacement functions of (i) step, (ii) sine, and (iii) triangle were utilized for the needle tip to follow in the air. For comparison, the displacement function period was kept the same; however, since the EM tracker was capable of measuring higher deflection angles, the maximum deflection angle was set to 20 degrees. It was assumed that the difference in maximum angle would not greatly inhibit the function of the controller since the period was sufficiently long. The same method was used for data collection, analysis, and comparison. Fig. 10a shows the controlled response of the FS with respect to the input functions, while Fig. 10b shows the corresponding absolute difference (bending angle error) between the measured output and desired input.

In a recent prior study [55], we measured the needle insertion force within our phantoms. The findings indicated an average needle insertion force of 14N within a tissue phantom with a stiffness of 77.14 ± 0.44 kPa. This result closely aligns with the 15.6N needle insertion force observed in in-vivo needle insertion experiments, as reported in ref. [71], during actual prostate brachytherapy procedures. This comparison underscores the ability of the active needle to effectively penetrate and bend within phantoms designed to mimic human tissue properties.

It is important to ensure robustness through repeated experimentation. The experiments conducted in this work have shown promising results to improve control response of the system. The noisy feedback of the EM tracking system and the detecting space of the US tracking system are subject to improvements. It is expected to conduct additional experiments to further validate the findings and enhance the reliability of the results. This will include performing repeated trials to assess the consistency and reproducibility of our measurements.

4. Discussions

While direct comparison between US tracking system and EM tracking system in two different mediums is not possible because of different control variables, this section provides a discussion of the findings

Table II. *Bending angle tracking error in closed-loop control of the active needle using the feedback received from ultrasound (US) and electromagnetic (EM) tracking systems. Units are in degrees.*

Input Function	Tracking Method	Min. Error	Max. Error	Mean Error
Sine	US	1e-04	1.09	0.23
	EM	6e-04	4.54	1.00
Triangle	US	1e-04	1.42	0.21
	EM	8e-04	3.97	0.96
Step (ignoring delay)	US	4e-04	11.45 (2.33)	2.00 (0.27)
	EM	10e-04	22.91 (4.02)	4.51 (0.83)

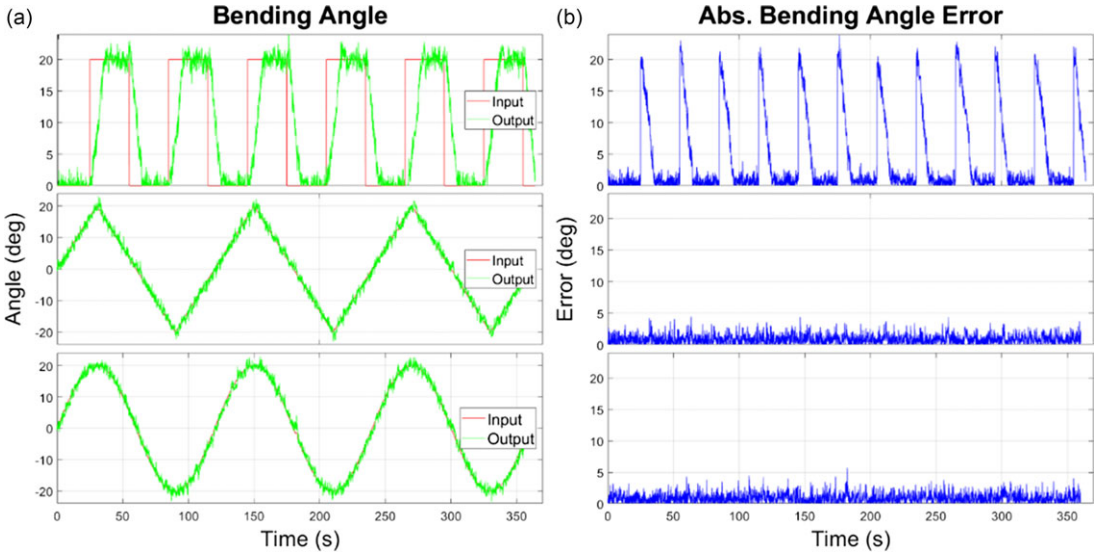

Figure 10. *Bending angle of the tendon-driven active needle: (a) Calculated from the data collected by the EM tracking system for the different input functions, and (b) Corresponding absolute difference (bending angle error) with respect to time.*

outlined in the two previous sections. The EM tracking system produced similar position data to the US tracking; however, there was significantly more noise in the data. The angular deflection measurements with the EM tracker fluctuated routinely around ±2.0 degrees for very close data points, whereas the US tracking measurements hardly fluctuated (±0.5 degrees).

Table 2 lists the maximum, minimum, and mean errors for each input displacement function (i.e., sine, triangle, and step) using US and EM tracking systems. The controller was able to realize a sine displacement function with mean error values of 0.23 and 1.00 degrees with US and EM tracking systems, respectively. Tracking the triangular displacement function was done with 0.21 and 0.96 degrees of mean error values for the US and EM tracking systems, respectively. It was however noticed that the actuation system was incapable of producing a quick response for the step displacement function, and thereby a delayed response. Due to the relatively slow ramp-up time, mean error values were 2.00 and 4.51 degrees for the US and EM tracking systems, respectively. The highest maximum absolute error was observed to be 22.91 degrees from the EM tracking system following step function with the lowest coming from the sine function with the US system (1.09 degrees). Because of the high absolute error, the largest mean error was also observed in the EM tracking step function with 4.51 degrees, and the lowest mean error was 0.21 degrees from the US tracking triangle function. The values in parentheses

were estimated for the step function when ignoring the delay period where the motors are running significantly behind the step. Once the measured angle was within the 10% of the desired step angle for the first time, data recording was resumed. The average delay period using the aforementioned parameters was 8.43 and 9.69 s for the US tracking and EM tracking systems, respectively. Ignoring the delay period, tracking of the step function resulted in mean error values of 0.27 and 0.83 degrees for the US and EM tracking systems, respectively, which closely align with the accuracies produced by the other displacement functions.

The mean error difference in tracking the desired bending angle of the active using the US or EM tracking systems were 0.77, 0.75, and 0.56 degrees for the sine, triangle, and step functions, respectively. The US tracking system realized a more accurate tracking of the active needle (average of 0.69 degrees improvement in accuracy) compared to the EM tracking for the three input functions used in this work. The results show that the US tracking system, submerged in the water, provides reliable feedback to the controller to realize a desired angular bending at the FS of the active needle with reasonable accuracy.

5. Conclusions

This work presents a closed-loop control of a bidirectional tendon-driven active needle in water medium and air using US and EM tracking, respectively. It has been observed that the bending angle of the active needle could be controlled using position feedback of the US or the EM tracking system with corresponding absolute difference (bending angle error) $<\pm 1$ degrees, and thereby comparable precisions. Therefore, the controller has been able to realize a desired bending angle at the FS of the active needle with reasonable accuracy using the US tracking system.

The US tracking system developed in this work resembles the tracking approach commonly employed in needle-based procedures for prostate interventions. It was shown that the controller is able to realize a desired bending angle at the FS of the active needle using the feedback of the US tracking system submerged in the water bath. This study marks the initial stride toward employing actively tendon-driven needles in prostate interventions, wherein both the needle and the US operate within the tissue.

Future work will focus on developing a closed-loop control to steer the active tendon-driven needle in a curved trajectory inside the prostate gland. Model-based control of the needle insertions integrating our recently developed model [54] and the findings of this work to reach targets deep inside the tissue is also among our future aims.

Author contributions. BK conceived and designed the study and simulated the control system. SL and BP carried out experiments, conducted data collection, and performed statistical analyses. SL and BK wrote the article.

Financial support. Research reported in this publication was supported by the National Institute of Biomedical Imaging and Bioengineering of the National Institutes of Health under Award Number K25EB030562. The content is solely the responsibility of the authors and does not necessarily represent the official views of the National Institutes of Health.

Competing interests. The authors declare no conflicts of interest exist.

Ethical standards. None.

References

[1] N. N. Stone, J. Roy, S. Hong, Y.-C. Lo and R. G. Stock, "Prostate gland motion and deformation caused by needle placement during brachytherapy," *Brachytherapy* **1**(3), 154–160 (2002). doi: 10.1016/S1538-4721(02)00058-2.

[2] S. Keereweer, J. D. F. Kerrebijn, P. B. A. A. van Driel, B. Xie, E. L. Kaijzel, T. J. A. Snoeks, I. Que, M. Hutteman, J. R. van der Vorst, J. S. D. Mieog, A. L. Vahrmeijer, C. J. H. van de Velde, R. J. Baatenburg de Jong and C. W. G. M. Löwik, "Optical image-guided surgery—Where do we stand?," *Mol Imag Bio* **13**(2), 199–207 (2011). doi: 10.1007/s11307-010-0373-2.

[3] "USCS Data Visualizations" Centers for Disease Control; and Prevention (2023). https://gis.cdc.gov/Cancer/USCS/#/AtAGlance/.

[4] Explore Cancer Statistics, American Cancer Society (ACS), cancer statistics center (2023).

[5] M. Fatyga, J. F. Williamson, N. Dogan, D. Todor, J. V. Siebers, R. George, I. Barani and M. Hagan, "A comparison of HDR brachytherapy and IMRT techniques for dose escalation in prostate cancer: A radiobiological modeling study," *Med Phys* **36**(9Part1), 3995–4006 (2009). doi: 10.1118/1.3187224.

[6] J. Hermesse, S. Biver, N. Jansen, E. Lenaerts, N. De Patoul, S. Vynckier, P. Coucke, P. Scalliet and P. Nickers, "A dosimetric selectivity intercomparison of HDR brachytherapy, IMRT and helical tomotherapy in prostate cancer radiotherapy," *Strahlentherapie und Onkol* **185**(11), 736–742 (2009). doi: 10.1007/s00066-009-2009-5.

[7] A. Challapalli, E. Jones, C. Harvey, G. O. Hellawell and S. A. Mangar, "High dose rate prostate brachytherapy: An overview of the rationale, experience and emerging applications in the treatment of prostate cancer," *British J Radiol* **85**(special_issue_1), S18–S27 (2012). doi: 10.1259/bjr/15403217.

[8] J. Skowronek, "Brachytherapy in the therapy of prostate cancer - an interesting choice," *Wspolczesna Onkol* **17**(5), 407–412 (2013). doi: 10.5114/wo.2013.38557.

[9] M. R. Cooperberg, D. P. Lubeck, M. V. Meng, S. S. Mehta and P. R. Carroll, "The changing face of low-risk prostate cancer: Trends in clinical presentation and primary management," *J Clin Oncol* **22**(11), 2141–2149 (2004). doi: 10.1200/JCO.2004.10.062.

[10] N. G. Thaker, T. N. Ali, M. E. Porter, T. W. Feeley, R. S. Kaplan and S. J. Frank, "Communicating value in health care using radar charts: A case study of prostate cancer," *J Oncol Pract* **12**(9), 813–820 (2016). doi: 10.1200/JOP.2016.011320.

[11] J. P. Ciezki, M. Weller, C. A. Reddy, J. Kittel, H. Singh, R. Tendulkar, K. L. Stephans, J. Ulchaker, K. Angermeier, A. Stephenson, S. Campbell, G.-P. Haber and E. A. Klein, "A comparison between low-dose-rate brachytherapy with or without androgen deprivation, external beam radiation therapy with or without androgen deprivation, and radical prostatectomy with or without adjuvant or salvage radiation therapy for high-risk prostate cancer," *Int J Radiat Oncol Biol Phys* **97**(5), 962–975 (2016). doi: 10.1016/j.ijrobp.2016.12.014.

[12] A. U. Kishan, T. Shaikh, P.-C. Wang, R. E. Reiter, J. Said, G. Raghavan, N. G. Nickols, W. J. Aronson, A. Sadeghi, M. Kamrava, D. J. Demanes, M. L. Steinberg, E. M. Horwitz, P. A. Kupelian and C. R. King, "Clinical outcomes for patients with Gleason score 9-10 prostate adenocarcinoma treated with radiotherapy or radical prostatectomy: A multi-institutional comparative analysis," *Eur Urol* **71**(5), 766–773 (2017). doi: 10.1016/j.eururo.2016.06.046.

[13] C. Shah, T. B. Lanni, M. I. Ghilezan, G. S. Gustafson, K. S. Marvin, H. Ye, F. A. Vicini and A. A. Martinez, "Brachytherapy provides comparable outcomes and improved cost-effectiveness in the treatment of low/intermediate prostate cancer," *Brachytherapy* **11**(6), 441–445 (2012). doi: 10.1016/j.brachy.2012.04.002.

[14] A. A. Laviana, A. M. Ilg, D. Veruttipong, H-Jui Tan, M. A. Burke, D. R. Niedzwiecki, P. A. Kupelian, C. R. King, M. L. Steinberg, C. R. Kundavaram, M. Kamrava, A. L. Kaplan, A. K. Moriarity, W. Hsu, D. J. A. Margolis, J. C. Hu and C. S. Saigal, "Utilizing time-driven activity-based costing to understand the short- and long-term costs of treating localized, low-risk prostate cancer," *Cancer* **122**(3), 447–455 (2016). doi: 10.1002/cncr.29743.

[15] K. Wallner, W. Ellis, K. Russell, W. Cavanagh and J. Blasko, "Use of TRUS to predict pubic arch interference of prostate brachytherapy," *Int J Radiat Oncol Biol Phys* **43**(3), 583–585 (1999). doi: 10.1016/S0360-3016(98)00459-3.

[16] P. Nickers, B. Thissen, N. Jansen and J. M. Deneufbourg, "192Ir or 125I prostate brachytherapy as a boost to external beam radiotherapy in locally advanced prostatic cancer: A dosimetric point of view," *Radiother Oncol* **78**(1), 47–52 (2006). doi: 10.1016/j.radonc.2005.09.002.

[17] J. Bellon, K. Wallner, W. Ellis, K. Russell, W. Cavanagh and J. Blasko, "Use of pelvic CT scanning to evaluate pubic arch interference of transperineal prostate brachytherapy," *Int J Radiat Oncol Biol Phys* **43**(3), 579–581 (1999). doi: 10.1016/S0360-3016(98)00466-0.

[18] S. A. Tincher, R. Y. Kim, M. P. Ezekiel, T. Zinsli, J. B. Fiveash, D. A. Raben, A. J. Bueschen and D. A. Urban, "Effects of pelvic rotation and needle angle on pubic arch interference during transperineal prostate implants," *Int J Radiat Oncol Biol Phys* **47**(2), 361–363 (2000). doi: 10.1016/S0360-3016(00)00434-X.

[19] B. Ryu, J. Bax, C. Edirisinge, C. Lewis, J. Chen, D. D'Souza, A. Fenster and E. Wong, "Prostate brachytherapy with oblique needles to treat large glands and overcome pubic arch interference," *Int J Radiat Oncol Biol Phys* **83**(5), 1463–1472 (2012). doi: 10.1016/j.ijrobp.2011.10.012.

[20] B. Konh, B. Padasdao, Z. Batsaikhan and J. Lederer, "Steering a Tendon-Driven Needle in High-Dose-Rate Prostate Brachytherapy for Patients with Pubic Arch Interference," **In:** *International Symposium on Medical Robotics (ISMR)*, (2021) pp. 1–7.

[21] B. Padasdao, Z. Batsaikhan, S. Lafreniere, M. Rabiei and B. Konh, "Modeling and Operator Control of a Robotic Tool for Bidirectional Manipulation in Targeted Prostate Biopsy," **In:** *International Symposium on Medical Robotics (ISMR)*, (2022) pp. 1–7.

[22] M. J. Zelefsky, Y. Yamada, G. Cohen, E. S. Venkatraman, A. Y. C. Fung, E. Furhang, D. Silvern and M. Zaider, "Postimplantation dosimetric analysis of permanent transperineal prostate implantation: Improved dose distributions with an intraoperative computer-optimized conformal planning technique," *Int J Radiat Oncol Biol Phys* **48**(2), 601–608 (2000).

[23] R. Podder, Y. Zheng, B. Konh, K. Lyons, T. Biswas, R. Ove, B. Traughber and T. K. Podder, "Curvilinear-Needle Implantation: A New Technique for Prostate HDR Brachytherapy," **In:** *AAPM 65th Annual Meeting & Exhibition*, (2023).

[24] B. Padasdao, R. Imanaka, T. K. Podder and B. Konh, "Curvilinear catheter implantation in HDR prostate brachytherapy: feasibility study," *Medical Physics*, (2024). Epub ahead of print, 14 pages doi: 10.1002/mp.17113.

[25] O. A. Bobrenkov, J. Lee and W. Park, "A new geometry-based plan for inserting flexible needles to reach multiple targets," *Robotica* **32**(6), 985–1004 (2014). doi: 10.1017/S0263574713001161.

[26] B. Huo, X. Zhao, J. Han and W. Xu, "Closed-loop control of bevel-tip needles based on path planning," *Robotica* **36**(12), 1857–1873 (2018). doi: 10.1017/S0263574718000772.

[27] R. Zhang, D. Xie, C. Qian, X. Duan and C. Li, "Design of a flexible robot toward transbronchial lung biopsy," *Robotica* **41**(3), 1055–1065 (2023). doi: 10.1017/S0263574722001345.

[28] Q. Xiao, X. Yang and Y. Chen, "Curvature-based force estimation for an elastic tube," *Robotica* **41**(6), 1749–1761 (2023). doi: 10.1017/S0263574723000115.

[29] B. Konh, D. Sasaki, T. K. Podder and H. Ashrafiuon, "3D manipulation of an active steerable needle via actuation of multiple SMA wires," *Robotica* **38**(3), 410–426 (2019). doi: 10.1017/S0263574719000705.

[30] F. Liang, B. J. Traughber, T. Biswas, G. Guo, R. F. Muzic and T. K. Podder, "Coordinated control of a 3DOF cartesian robot and a shape memory alloy-actuated flexible needle for surgical interventions: A non-model-based control method," *Robotica* **40**(6), 1695–1712 (2022). doi: 10.1017/S0263574721001314.

[31] J. Burgner-Kahrs, D. C. Rucker and H. Choset, "Continuum robots for medical applications: A survey," *IEEE Trans Robot* **31**(6), 1261–1280 (2015). doi: 10.1109/TRO.2015.2489500.

[32] T. E. Ertop, J. F. d' Almeida, E. Amanov, J. Shrand, N. Nimmagadda, S. Setia, N. L. Kavoussi, S. D. Herrell and R. J. Webster, "Towards Suturing from Within the Urethra Using Concentric Tube Robots: First Experiences in Biological Tissues," **In:** *2022 International Symposium on Medical Robotics (ISMR)*, 2022) pp. 1–5. doi: 10.1109/ISMR48347.2022.9807548.

[33] J. B. Gafford, S. Webster, N. Dillon, E. Blum, R. Hendrick, F. Maldonado, E. A. Gillaspie, O. B. Rickman, S. D. Herrell, R. J. Webster, "A concentric tube robot system for rigid bronchoscopy: A feasibility study on central airway obstruction removal," *Ann Biomed Eng* **48**(1), 181–191 (2020). doi: 10.1007/s10439-019-02325-x.

[34] Z. K. Varnamkhasti and B. Konh,"Design, Fabrication, and testing of a flexible three-dimensional printed percutaneous needle with embedded actuators," *ASME J Med Devices* **15**(2), 021007 (2020).

[35] Z. K. Varnamkhasti and B. Konh, "Compact 3D-printed active flexible needle for percutaneous procedures," *Surg Innov* **27**(4), 402–405 (2020). doi: 10.1177/1553350620945564.

[36] M. Khadem, C. Rossa, N. Usmani, R. S. Sloboda and M. Tavakoli, "Introducing Notched Flexible Needles with Increased Deflection Curvature in Soft Tissue," **In:** *2016 IEEE International Conference on Advanced Intelligent Mechatronics (AIM)*, (2016) pp. 1186–1191. doi: 10.1109/AIM.2016.7576931.

[37] B. Padasdao, S. Lafreniere, M. Rabiei, Z. Batsaikhan and B. Konh, "Teleoperated and automated control of a robotic tool for targeted prostate biopsy," *J Med Robot Res* **8**(1&2), 2340002 (2023). doi: 10.1142/S2424905X23400020.

[38] S. Jeong, Y. Chitalia and J. P. Desai, "Design, modeling, and control of a coaxially aligned steerable (COAST) guidewire robot," *IEEE Robot Autom Lett* **5**(3), 4947–4954 (2020). doi: 10.1109/LRA.2020.3004782.

[39] A. Krieger, I. I. Iordachita, P. Guion, A. K. Singh, A. Kaushal, C. Menard, P. A. Pinto, K. Camphausen, G. Fichtinger and L. L. Whitcomb, "An MRI-compatible robotic system with hybrid tracking for MRI-guided prostate intervention," *IEEE Trans Biomed Eng* **58**(11), 3049–3060 (2011). doi: 10.1109/TBME.2011.2134096.

[40] S. Lafreniere, O. L. Sprouse, R. J. Padilla and B. Konh, "Design of an MRI-Compatible Robot for Image-Guided Needle Insertion Procedures Using Active Tendon-Driven needles," **In:** *Frontiers in Biomedical Devices, BIOMED - 2023 Design of Medical Devices Conference*, (2023).

[41] S. Lafreniere, "Design Consideration and Development of an MRI-Compatible Robot for Prostate Interventions," **In:** *Frontiers in Biomedical Devices, BIOMED - 2024 Design of Medical Devices Conference*, (2024) pp. 1–5.

[42] M. Khadem, C. Rossa, R. S. Sloboda, N. Usmani and M. Tavakoli, "Ultrasound-guided model predictive control of needle steering in biological tissue," *J Med Robot Res* **01**(01), 1640007 (2016). doi: 10.1142/s2424905x16400079.

[43] A. Haddadi and K. Hashtrudi-Zaad, "Development of a Dynamic Model for Bevel-Tip Flexible Needle Insertion into Soft Tissues," **In:** *2011 Annual International Conference of the IEEE Engineering in Medicine and Biology Society*, (2011) pp.7478–7482. doi: 10.1109/IEMBS.2011.6091845.

[44] A. Haddadi, O. Goksel, S. E. Salcudean and K. Hashtrudi-Zaad, "On the Controllability of Dynamic Model-Based Needle Insertion in Soft Tissue," **In:***2010 Annual International Conference of the IEEE Engineering in Medicine and Biology*, (2010) pp. 2287–2291. doi: 10.1109/IEMBS.2010.5627676.

[45] M. Mahvash and P. E. Dupont, "Mechanics of dynamic needle insertion into a biological material," *IEEE Trans Biomed Eng* **57**(4), 934–943 (2010). doi: 10.1109/TBME.2009.2036856.

[46] R. J. Roesthuis, M. Abayazid and S. Misra, "Mechanics-Based Model for Predicting in-Plane Needle Deflection with Multiple Bends," **In:** *2012 4th IEEE RAS & EMBS International Conference on Biomedical Robotics and Biomechatronics (BioRob)*, (2012) pp. 69–74. doi: 10.1109/BioRob.2012.6290829.

[47] M. Khadem, B. Fallahi, C. Rossa, R. S. Sloboda, N. Usmani and M. Tavakoli, "A Mechanics-Based Model for Simulation and Control of Flexible Needle Insertion in Soft Tissue," **In:** *2015 IEEE International Conference on Robotics and Automation (ICRA)*, (2015) pp. 2264–2269. doi: 10.1109/ICRA.2015.7139499.

[48] T. Lehmann, C. Rossa, N. Usmani, R. S. Sloboda and M. Tavakoli, "A real-time estimator for needle deflection during insertion into soft tissue based on adaptive modeling of needle-tissue interactions," *IEEE/ASME Trans Mechatr* **21**(6), 2601–2612 (2016). doi: 10.1109/TMECH.2016.2598701.

[49] C. Rossa, M. Khadem, R. Sloboda, N. Usmani and M. Tavakoli, "Adaptive quasi-static modelling of needle deflection during steering in soft tissue," *IEEE Robot Autom Lett* **1**(2), 916–923 (2016). doi: 10.1109/LRA.2016.2527065.

[50] O. Goksel, S. E. Salcudean and S. P. Dimaio, "3D simulation of needle-tissue interaction with application to prostate brachytherapy," *Comput Aided Surg* **11**(6), 279–288 (2006). doi: 10.3109/10929080601089997.

[51] O. Goksel, E. Dehghan and S. E. Salcudean, "Modeling and simulation of flexible needles," *Med Eng Phys* **31**(9), 1069–1078 (2009). doi: 10.1016/j.medengphy.2009.07.007.

[52] R. J. Webster III, J. S. Kim, N. J. Cowan, G. S. Chirikjian and A. M. Okamura, "Nonholonomic modeling of needle steering," *Int J Rob Res* **25**(5-6), 509–525 (2006). doi: 10.1177/0278364906065388.

[53] B. Fallahi, M. Khadem, C. Rossa, R. Sloboda, N. Usmani and M. Tavakoli, "Extended Bicycle Model for Needle Steering in Soft Tissue," **In:** *2015 IEEE/RSJ International Conference on Intelligent Robots and Systems (IROS)*, (2015) pp. 4375–4380. doi: 10.1109/IROS.2015.7353998.
[54] B. Padasdao and B. Konh, "A model to predict deflection of an active tendon-driven notched needle inside soft tissue," *J Eng Sci Med Diagnostics Ther* **7**(1), 011006 (2024). doi: 10.1115/1.4063205.
[55] B. Padasdao and B. Konh, "A mechanics-based model for a tendon-driven active needle navigating inside a multiple-layer tissue," *J Robot Surg* **18**(1), 146 (2024). doi: 10.1007/s11701-024-01900-2.
[56] B. Padasdao, Z. K. Varnamkhasti and B. Konh, "3D steerable biopsy needle with a motorized manipulation system and ultrasound tracking to navigate inside tissue," *J Med Robot Res* **5**(03n04), 2150003 (2020). doi: 10.1142/S2424905X21500033.
[57] M. Khadem, C. Rossa, N. Usmani, R. S. Sloboda and M. Tavakoli, "Semi-automated needle steering in biological tissue using an ultrasound-based deflection predictor," *Ann Biomed Eng* **45**(4), 924–938 (2017). doi: 10.1007/s10439-016-1736-x.
[58] G. J. Vrooijink, M. Abayazid, S. Patil, R. Alterovitz and S. Misra, "Needle path planning and steering in a three-dimensional non-static environment using two-dimensional ultrasound images," *Int J Rob Res* **33**(10), 1361–1374 (2014). doi: 10.1177/0278364914526627.
[59] B. Konh, B. Padasdao, Z. Batsaikhan and S. Y. Ko, "Integrating robot-assisted ultrasound tracking and 3D needle shape prediction for real-time tracking of the needle tip in needle steering procedures," *Int J Med Robot Comput Assist Surg* **17**(4), e2272 (2021). doi: 10.1002/rcs.2272.
[60] J. Carriere, C. Rossa, R. Sloboda, N. Usmani and M. Tavakoli, "Real-Time Needle Shape Prediction in Soft-Tissue Based on Image Segmentation and Particle Filtering," **In:** *2016 IEEE International Conference on Advanced Intelligent Mechatronics (AIM)*, (2016) pp. 1204–1209. doi: 10.1109/AIM.2016.7576934.
[61] B. Konh, Z. Batsaikhan and B. Padasdao, "3D Shape Estimation of an Active Needle Inside Tissue Using 2D Ultrasound Images," **In:** *Design of Medical Devices Conference*, (2021) pp. 1–4.
[62] T. A. Brumfiel, A. Sarma and J. P. Desai, "Towards FBG-based End-Effector Force Estimation for a Steerable Continuum Robot," **In:** *2022 International Symposium on Medical Robotics (ISMR)*, (2022) pp. 1–7.
[63] Y. Chitalia, N. J. Deaton, S. Jeong, N. Rahman and J. P. Desai, "Towards FBG-based shape sensing for micro-scale and meso-scale continuum robots with large deflection," *IEEE Robot Autom Lett* **5**(2), 1712–1719 (2020). doi: 10.1109/LRA.2020.2969934.
[64] S. Karimi and B. Konh, "Kinematics modelling and dynamics analysis of an SMA-actuated active flexible needle for feedback-controlled manipulation in phantom," *Med Eng Phys* **107**, 103846 (2022).
[65] S. Karimi and B. Konh, "Self-sensing feedback control of multiple interacting shape memory alloy actuators in a 3D steerable active needle," *J Intell Mater Syst Struct* **31**(12), 1524–1540 (2020).
[66] B. Padasdao and B. Konh, "Shape memory alloy actuators in an active needle - modeling, precise assembly, and performance evaluation," *J Manuf Sci Eng* **143**(2), 021003 (10 pages) (2020).
[67] B. Konh, P. Berkelman and S. Karimi, Needle tip manipulation and control of a 3D steerable SMA-activated flexible needle, (2020).
[68] B. Padasdao, S. Lafreniere, M. Rabiei, Z. Batsaikhan and B. Konh, "Teleoperated and automated control of a robotic tool for targeted prostate biopsy," *J Med Robot Res* **8**(1&2), 2340002–2340016 (2022).
[69] K. W. Eastwood, P. Francis, H. Azimian, A. Swarup, T. Looi, J. M. Drake and H. E. Naguib, "Design of a contact-aided compliant notched-tube joint for surgical manipulation in confined workspaces," *J Mech Robot* **10**(1), 1–12 (2018). doi: 10.1115/1.4038254.
[70] N. V. Datla, B. Konh, J. J. Y. Koo, D. J. W. Choi, Y. Yu, A. P. Dicker, T. K. Podder, K. Darvish and P. Hutapea, "Polyacrylamide phantom for self-actuating needle-tissue interaction studies," *Med Eng Phys* **36**(1), 140–145 (2014). doi: 10.1016/j.medengphy.2013.07.004.
[71] T. Podder, D. Clark, J. Sherman, D. Fuller, E. Messing, D. Rubens, J. Strang, R. Brasacchio, L. Liao, W.-S. Ng and Y. Yu, "In vivo motion and force measurement of surgical needle intervention during prostate brachytherapy," *Med Phys* **33**(8), 2915–2922 (2006). doi: 10.1118/1.2218061.

Cite this article: S. Lafreniere, B. Padasdao and B. Konh (2024). "Closed-loop control of a tendon-driven active needle for tip tracking at desired bending angle for high-dose-rate prostate brachytherapy", Robotica **42**, 2511–2527. https://doi.org/10.1017/S0263574724000900